Ultrasonic Wake-Up With Precharged Transducers

Angad S. Rekhi[ID], *Student Member, IEEE*, and Amin Arbabian, *Senior Member, IEEE*

Abstract—We present an ultralow-power millimeter-sized ultrasonic wake-up receiver (WuRx) that uses precharged ultrasonic transducers to wirelessly receive wake-up signatures. Our WuRx takes advantage of the low carrier frequency afforded by the low speed of sound to achieve high impedance, and thus high sensitivity, operation in a millimeter-sized form factor. We discuss the system-level considerations that arise from the use of ultrasound as a mode of signature transmission, including the choice of operating frequency and the effect of transducer miniaturization on WuRx sensitivity. We describe the design of the receiver electronics and support our case for ultrasonic wake-up with thorough wireless measurements of error rate and electrical characterization of multiple dice from the same wafer lot. The receiver electronics are fabricated in 65-nm CMOS technology, while the receiver transducer is fabricated by means of a custom in-house process. The receiver achieves a sensitivity of -59.7 dBm at a bit error rate (BER) of 10^{-3} with a power consumption of 8 nW and a footprint of 14.5 mm^2. Our benchmarking shows that the proposed WuRx achieves the lowest system area/aperture of all RF and acoustic WuRxs in the literature (1.45$\times$ smaller than the state of the art) while maintaining competitive sensitivity and power consumption.

Index Terms—Detector-first architecture, Internet of Things (IoT), millimeter-sized sensor, precharged transducer, ripple cancellation, ultralow-power, ultrasonic transducer, wake-up receiver (WuRx).

I. Introduction

THE number of connected devices worldwide is enormous and increasing [1]. A growing number of these devices are built for Internet of Things (IoT) applications, which include distributed sensing and edge computation [2]. At scale, these applications promise increased insight into our activities and surroundings; they therefore hold the potential for high societal impact. However, to achieve the requisite scale at an acceptable cost, a number of technological challenges must be addressed.

We focus on one very important technological challenge: extending the lifetime of small sensor nodes by means of wake-up receivers (WuRxs). As shown in Fig. 1, WuRxs are very-low-power circuits that listen for a specific wireless signature; upon receiving a signature, the node is turned

on [3]. By keeping the node off until needed, its battery life can be greatly extended, thus lessening required maintenance of sensor networks and improving their deployability. Over the past decade, WuRxs in the literature have progressed from simplified versions of cellular receivers to extremely streamlined circuits operating in subthreshold that are optimized for signature detection [4], [5]. This evolution in architecture has led to the improvement of sensitivity and power consumption by orders of magnitude, along with an accompanying increase in the number and size of off-chip components and a downward trend in carrier frequency (implying the need for a larger antenna) [6].

These trends have provided effective solutions for a number of important applications, but for settings that demand ubiquity and unobtrusiveness, the size of the WuRx is a critical third specification that must be co-optimized along with power and sensitivity. However, the footprint of prior WuRxs has increased in a way that is fundamentally tied to the use of sub-gigahertz or few-gigahertz electromagnetic waves as carriers of the wake-up signature, since efficiently extracting a signal from an antenna requires that the antenna size scale with the wavelength of operation [7]. Thus, with RF signature transmission, achieving our goal of a millimeter-sized form factor for the overall system would require working at mm-wave frequencies [8].

In this paper, we describe the design and operation of our ultrasonic WuRx. Our WuRx takes advantage of the orders of magnitude lower propagation velocity of acoustic waves relative to electromagnetic waves by operating in the kilohertz regime with a millimeter-sized radiator; this allows WuRx miniaturization, avoids the power and complexity overhead of mm-wave operation, and enables the co-design of a high-impedance interface between transducer and front-end circuitry, which leads to high-sensitivity operation. Although outside the scope of this paper, the advantages of ultrasonic operation extend to the transmitter — phased arrays working below 100 kHz can take advantage of commodity hardware and relatively efficient power amplification and distribution, leading to a substantial improvement in cost and power relative to RF or mm-wave arrays, which may require custom silicon design and relatively inefficient power distribution. This paper extends our earlier conference proceeding on the same topic by exploring circuit- and system-level concepts in greater detail and by presenting measurements of inter-die variation [9].

Fig. 2 shows a block diagram of the WuRx described in this paper. The incident ultrasonic signature is converted into an electrical signal by the highly sensitive ultrasonic transducer described in Section II. Section II also explains how the electrical properties of this transducer would change if further miniaturized. Once on the chip, the OOK signal is
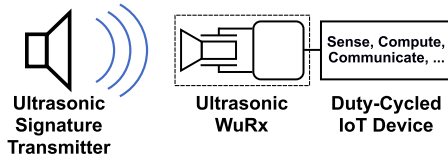
Fig. 1. Conceptual block diagram of ultrasonic signature transmission, propagation, and reception by an ultrasonic WuRx. The WuRx gates the operation of a duty-cycled IoT device.
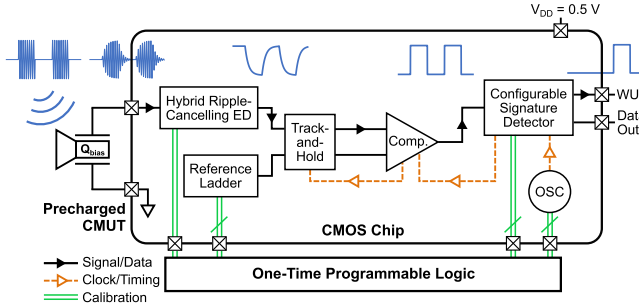

Fig. 2. Block diagram of the WuRx described in this paper. An incident acoustic signature results in a digital output wake-up signal.

demodulated with a ripple-cancelling envelope detector (ED), digitized, and compared to a hard-coded signature to determine whether to output the wake-up signal. Section III describes the operation of these circuits, and how they work with the transducer to enable the WuRx to achieve competitive sensitivity under a tight power and area budget while remaining robust to RF and ultrasonic interference. Section IV presents characterization and measurement results of the WuRx and compares it to previously published designs.

II. Ultrasound for Wake-Up

In this section, we first provide a short overview of acoustic propagation in free space. Then, after a brief introduction to acoustic transducers, capacitive micromachined ultrasonic transducers (CMUTs), and precharging, we present the results of our study in CMUT miniaturization undertaken using transducer modeling code (this code has been verified by past measurements). In particular, we show how miniaturization impacts system specifications such as sensitivity and noise.

A. Propagation

In the far field of a vibrating source, the intensity of the emitted acoustic radiation falls off as the square of the distance from the source, due to spreading loss; similar to RF far-field propagation, this spreading loss can be captured by Friis' equation. Acoustic waves also experience non-negligible absorption due to viscosity and relaxation processes, which can be modeled by an additional exponential attenuation factor that is dependent on environmental parameters such as temperature and relative humidity. Finally, the nonlinearity of the pressure-density relations and of the acoustic equations of motion lead to wave distortion and saturation at high amplitudes; we lump these effects into a single correction factor, γ_{NL}. The combined

effects of spreading loss, absorption, and nonlinearity upon the intensity I_{prop} at axial distance R from the source can thus be expressed by the following relation:

$$I_{\mathrm{prop}} = \gamma_{\mathrm{NL}} e^{-\alpha R} \frac{P_{\mathrm{Tx}} G_{\mathrm{Tx}}}{4\pi R^2}. \tag{1}$$

Here, P_{Tx} is the transmitted power, G_{Tx} is the transmitter gain, and α is the absorption coefficient. For simple transmitter shapes and low P_{Tx}, the correction factor γ_{NL} can be estimated from prior work, while for more complex shapes and/or higher P_{Tx}, acoustic wave simulations can be used to find γ_{NL} [10].

For a given WuRx sensitivity, the design variables governing the operating range are the transmitter shape, size, and output power. The choice of these variables is constrained by recommended maximum intensity limits set by OSHA in the USA and corresponding agencies around the world. In the face of incomplete research into the safety of airborne ultrasound, OSHA's recommended limit is 115 dB SPL over the frequency range of interest. To meet this limit, systems must either keep the generated ultrasonic intensity below 115 dB SPL everywhere, or else require users to maintain a minimum safe distance from the transmitter. For the measurements presented in Section IV, we follow the former approach.

B. Transducer

Acoustic transducers convert acoustic energy to electrical energy and vice versa. For air-coupled ultrasonic operation, membrane-based transducers, such as CMUTs and piezoelectric micromachined ultrasonic transducers (PMUTs), are attractive because of their ability to impedance match to air (which is difficult for bulk piezoelectric transducers). For WuRxs, only receive-mode characteristics are of interest; this is in contrast to, for instance, a pulse-echo-based imager, which requires optimization of both Rx- and Tx-mode characteristics. We work with CMUTs, which can be designed to have small gap sizes and thus excellent Rx sensitivities.

1) CMUT Background: A conventional CMUT consists of a capacitor with one movable plate that is anchored along its circumference. When the CMUT is biased with a dc voltage V_0, acoustic radiation incident on the transducer causes the movable plate to vibrate, creating a time-varying capacitance and accompanying electrical current, as predicted by the following equation [11]:

$$I = \frac{dQ}{dt} = \frac{d}{dt}[CV] = V_0 \frac{dC}{dt}. \tag{2}$$

While the equation above helps to convey the intuition behind CMUT operation, the time-varying capacitance must be quantitatively tied to the incident acoustic signal in order to find important system parameters such as sensitivity and bandwidth. To do so, it is common to model the movable plate as a mass-spring-damper system, with additional mass and damping terms contributed by the medium. This results in second-order differential equations, which can very naturally be represented as circuit diagrams. Fig. 3 shows a general CMUT circuit diagram. Two different physical domains— mechanical and electrical—are connected by voltage and current sources whose values partially depend on parameters from
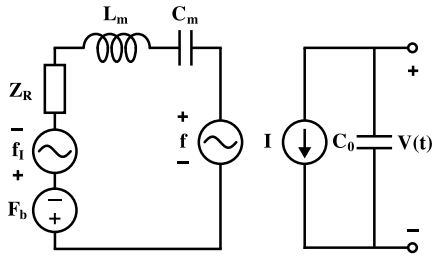
Fig. 3. General large-signal equivalent circuit model of CMUT: F_b is the static force on the membrane due to atmospheric pressure; f_I is the harmonic force due to an incident acoustic signal; Z_R is the radiation impedance of the device; C_m and L_m are, respectively, the compliance and the mass of the membrane; f is the net force on the membrane; I is the transducer current due to time-varying capacitance; and C_0 is the capacitance of the CMUT with zero membrane displacement. Full details available in [11].
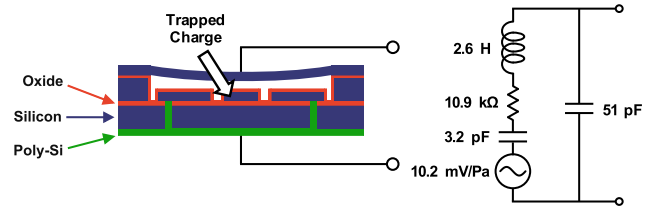

Fig. 4. Cross-sectional diagram of precharged CMUT in hand (not to scale) (left); its Rx-mode equivalent all-electrical circuit model (right).
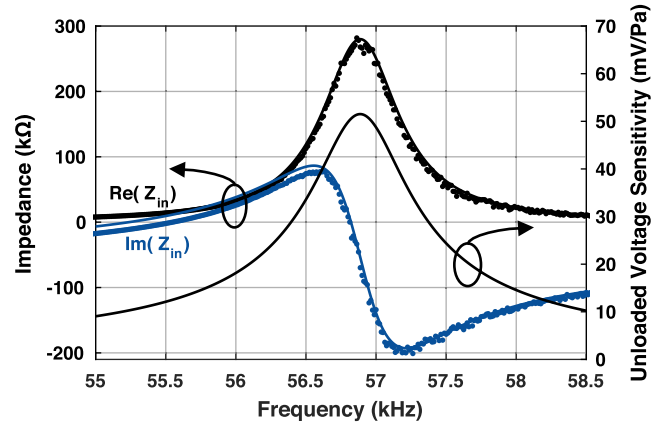

Fig. 5. Measured and best-fit impedance, and best-fit receive sensitivity of precharged CMUT in hand.

the other physical domain. Reference [11] derives and analyzes this circuit model in detail, validating it with measured results.

As (2) shows, conventional CMUTs produce no electrical output signal if no bias voltage is provided (i.e., if $V_0 = 0$); moreover, the output current grows with the bias voltage for a given change in capacitance (i.e., incident acoustic radiation). Therefore, CMUTs can require a large voltage bias to function as sensitive transducers in air, often reaching high 10s—low 100sV [12]. Provision of this dc bias can be incompatible with the area and power requirements of next-generation IoT nodes, as it would require at least a power source, dc–dc conversion, and voltage regulation. For our WuRx, we instead use a precharged CMUT, which is biased using charge stored on an isolated island carved out of the non-movable plate of the transducer; the charge biasing is performed only once, after fabrication of the device [13]. The trapped charge obviates the need for a dc bias voltage; moreover, it can be modeled by a dc voltage source in series with the transducer [14].

In this paper, we use one of the previously fabricated precharged transducers described in [13]. These transducers have been shown to retain their charge over a span of several years and have been previously used for applications in wireless power recovery [10]. To obtain an electrical model of the transducer, we start with the general CMUT circuit diagram, linearize around the bias point, and bring all elements into the electrical domain; then, we measure the transducer's electrical impedance and receive-mode sensitivity, and use those measurements to derive best-fit component values. The resultant all-electrical circuit model of the precharged CMUT in hand is shown in Fig. 4, which also shows a cross-sectional diagram of the precharged device. Measured and best-fit impedance, and best-fit sensitivity, are plotted in Fig. 5.

With CMUT in hand, the frequency of operation should be chosen to minimize the incident acoustic power required for reliable wake-up. When choosing the frequency, we assume this incident power is frequency independent; this ignores propagative effects, which is a reasonable simplification for the narrow frequency range over which the CMUT is most sensitive [10]. The optimal frequency is dependent on the overall function and specifications of the WuRx, and it is instructive to briefly contrast WuRxs with other types of

systems to clarify the tradeoffs involved. For instance, in power-harvesting systems, the transducer impedance must be matched to by the circuitry to extract maximum power (either with a conjugate match, or with a power match, if matching components are lossy [7], [15]). Thus, it can be beneficial to operate in the inductive regime of the transducer in order to resonate with the capacitance of the downstream matching network or rectifier [16], or to operate at series resonance if the rectifier impedance cannot be transformed high enough to achieve an impedance match in the inductive regime [10].

For receiver systems like our WuRx, impedance matching at every interface, including at the CMUT–CMOS interface, maximizes the available SNR. However, the low-power (<10 nW), low-frequency (<100 kHz) operation of our circuit leads to input impedances greater than 10 MΩ, while the CMUT impedance is no greater than $\sim$300-kΩ at any frequency (see Fig. 5). Moreover, efficiently matching between these two impedance levels under our strict power and area budgets is prohibitive. Therefore, we directly connect the CMUT to the on-chip front end and operate at argmax(Re{Z_trans}), which gets as close to an impedance match as possible.

2) CMUT Optimization: Having reviewed how to choose the frequency of operation for a CMUT in hand, we now investigate the design of the transducer itself. The results of this investigation do not factor into the measurements presented in Section IV, which are based on an existing transducer. Instead, the study in CMUT design that follows is meant to explore to what extent future ultrasonic WuRxs can be miniaturized, since the size of the CMUT currently limits the size of the WuRx [9].

To constrain the design space, we start with the precharged CMUT in hand and sweep key design parameters with the aim of decreasing transducer area while keeping the operation frequency constant; this emulates the need for a drop-in WuRx replacement that must be backward compatible and avoids complicating the design of the CMUT due to frequency-dependent propagation effects. For this paper, the design parameters we explore are the CMUT radius, the thickness of the top plate, and the height of the gap between the plates. In general, decreasing the radius of the device by itself increases its resonance frequency; as will be shown below, its top plate can be thinned in order to compensate, but together these changes have a deleterious effect on the sensitivity of the device and, therefore, of the WuRx. The precise area-sensitivity tradeoff that this results in is discussed in detail below.

Our procedure is to write custom MATLAB optimizer functions that call MATLAB-based CMUT design code [17], and using these functions, explore two methods to reduce the CMUT area while keeping the operation frequency constant. At every radius, method 1 minimizes the absolute difference between desired and actual operation frequencies by letting the plate thickness vary, while method 2 optimizes for both frequency accuracy and maximum sensitivity (using a suitably defined cost function) by letting both plate thickness and gap height vary. Both methods assume constant aperture efficiency over design parameters; more accurate results can be obtained by accounting for air and support losses as functions of plate thickness and area [18]. They also assume that the bias charge corresponds to a bias voltage that is a fixed fraction of the collapse voltage, since the bias charge can be increased to improve sensitivity at the expense of dynamic range at any given point in the design space.

Fig. 6 shows the results of both methods. Most notably, method 1 is limited by the fact that reducing the device radius below 1.6 mm causes the top plate to collapse even with no applied bias, which would make sensitive operation at the desired frequency impossible. This happens because the gap is held constant, and it implies that method 1 considers too restrictive a design space. Method 2 overcomes this restriction, and we use it to drive down to a radius of 0.75 mm; this is a 72% reduction in system (CMOS + CMUT) area. Above 1.6 mm, both methods provide similar results. We now discuss the results in greater detail.

We find that as the device radius a is reduced linearly, the plate thickness t drops quadratically to keep the operation frequency constant; this is expected based on the fact that the resonance frequency of a thin plate is proportional to t/a^2 [17, p. 14]. Method 1 keeps the frequency within a ± 20 Hz threshold of the operation frequency for the CMUT in hand, while method 2 has a slightly looser tolerance of ± 70 Hz; this can be tightened at the expense of optimization runtime.

The available power for a constant incident intensity falls quadratically as the radius is reduced linearly. Because $P_{av} \propto S_{Rx}^2/\mathrm{Re}\{Z_{in}\}$, in theory, this leaves many possibilities for how S_{Rx} and $\mathrm{Re}\{Z_{in}\}$ will vary with radius. Our optimization shows that both S_{Rx} and $\mathrm{Re}\{Z_{in}\}$ fall with decreasing radius and are
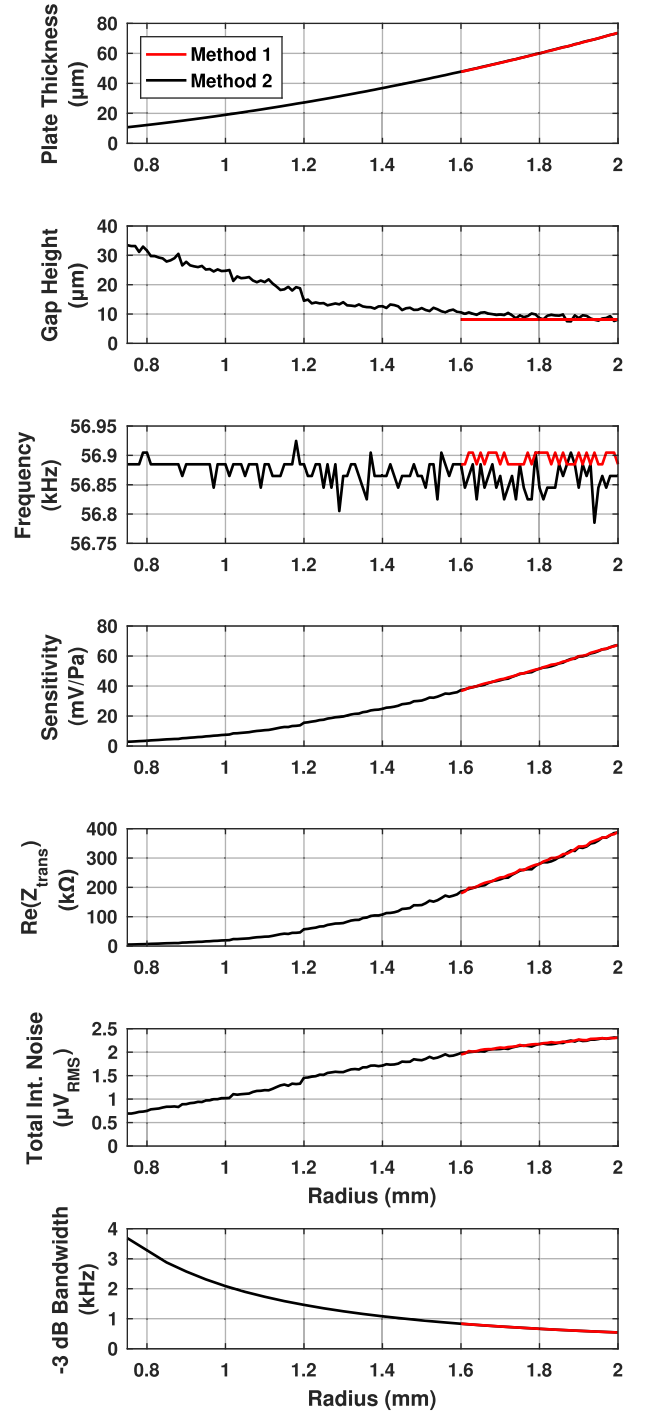

Fig. 6.   Results of CMUT design optimization.

convex. We emphasize that as the CMUT area decreases and its gap increases, the real part of its impedance *decreases*, unlike what would be expected of the impedance of a non-radiative capacitor. This highlights the difference between a CMUT and a regular capacitor—the former is an acoustic radiator, the latter a non-radiative energy storage element (ignoring electromagnetic radiation at these frequencies). Note the similarity to a small loop antenna, whose radiation resistance also decreases with decreasing loop area [19, p. 238]. Fig. 6 also shows the rms total integrated noise (TIN) at
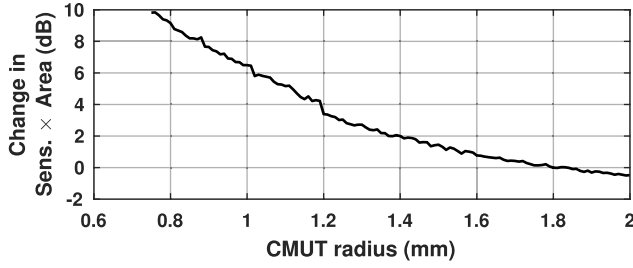
Fig. 7. Change in Sensitivity · Area with changing CMUT radius, as found by CMUT design optimization.

Fig. 8. Frequency-ripple tradeoff for different ED topologies (simulated).

the output, which can be shown to be $(C_S/C_P) \cdot kT/(C_S+C_P)$. In this WuRx system, the bandwidth of the noise is set by the narrowband (NB) ($Q \sim 90$) transducer, not the more broadband front-end circuitry, so it makes sense to consider the TIN rather than the spot noise at the transducer output. The TIN falls with decreasing radius, which agrees with the fact that Re$\{Z_{in}\}$ also falls with decreasing radius, as per the fluctuation-dissipation theorem [20]. Finally, Fig. 6 also shows that the bandwidth of the transducer rises as the transducer is made smaller, as might be expected from the sensitivity-bandwidth tradeoff often observed in CMUT design; in this case, the bandwidth rises because the mass and spring constant of the vibrating plate fall faster than the transducer's radiation resistance as it is miniaturized [17]. Note that the WuRx circuit is broadband; higher CMUT bandwidth just makes it easier for the transmitter to find the optimal carrier frequency of operation if it is not known *a priori*.

Our optimization shows that the overall system size could be reduced by at least 72% by fabricating and precharging a CMUT with a smaller radius, thinner plate, and larger gap height, all while keeping the operation frequency constant, but that this reduction in CMUT area comes with a concomitant decrease in radiation resistance. Because $P_{min} \propto V_{min}^2/\text{Re}\{Z_{in}\}$ and V_{min} is determined by the bit error rate (BER) specification (as discussed in Section III), decreasing Re$\{Z_{in}\}$ leads to poorer sensitivity. The resultant change in Sensitivity · Area is shown in Fig. 7. Interestingly, with our CMUT design optimization procedure, Re$\{Z_{in}\}$ changes superlinearly with the area, so that Sensitivity · Area increases (worsens) with decreasing area. The impact of area reduction on operation range would be even more severe, since the minimum required intensity is inversely proportional to the product of Re$\{Z_{in}\}$ and area, both of which decrease with decreasing area. These findings speak to the challenges of WuRx miniaturization in general, and in particular, show that without additional power expenditure in the front end, further transducer miniaturization comes at the cost of WuRx sensitivity.

III. CIRCUIT DESIGN

A. Front End

We pursued an ED-first architecture in order to avoid having to provide potentially power-hungry gain at the carrier frequency; we explore this choice further in the Appendix. The simplest and most power-efficient ED topologies for relatively low required conversion gain (which, for an ED, is the ratio
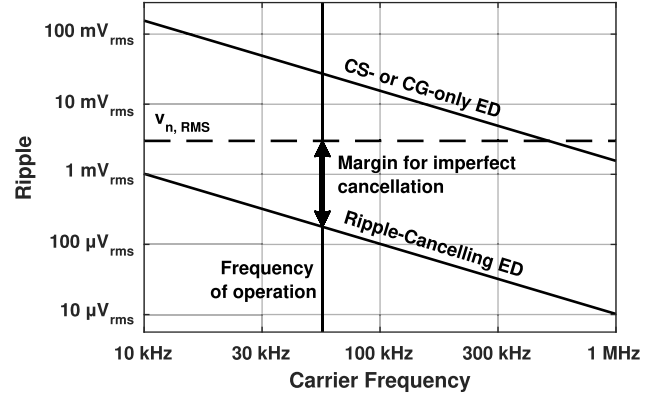
of output signal amplitude at dc to input signal amplitude at the carrier) are single-stage topologies operated in sub-threshold [21]. We began by considering the common-source (CS) stage. The exponential I–V relationship of a MOSFET in subthreshold leads to a component of the drain current at dc that is proportional to the square of the ac input voltage. Meanwhile, the standard linear gain from input to output results in output ripple at the carrier, which can hamper the sensitivity of the WuRx if large enough. Thus, filtering the output of the ED is required, which creates a tradeoff between sensitivity and data rate. For an RF-based WuRx with relatively low (<1 kbit/s) data rate, the carrier frequency and the data bandwidth differ by several orders of magnitude, so a simple single-pole filter can push the output ripple below the noise level [5]. For an ultrasound-based WuRx, working with the same filter at the same output ripple level would require settling for a data bandwidth that is smaller than the carrier frequency by the same ratio—this would result in a data rate of 0.15 bit/s, which is impractical even for an infrequently activated WuRx. Moreover, more sophisticated ED ripple reduction techniques would exceed the power budget allocated to the front end.

We address this problem by using the fact that the conversion gains of both the CS and common-gate (CG) ED stages have the same polarity, despite their standard linear gains having opposite sign. Thus, for roughly double the power of one single-FET ED stage, the outputs of these two stages can be combined to partially cancel the ripple at the fundamental while reinforcing the resultant dc current. This results in a data rate comparable to RF-based WuRxs with similar front-end power consumption, despite the drastically lower carrier frequency. Fig. 8 shows how this scheme improves the tradeoff between carrier frequency and output ripple. Fig. 9 shows a simplified schematic of this stage. PMOS-based pseudoresistors are used throughout the design for both biasing (R_{bias1}–R_{bias5}) and averaging (R_{avg1} and R_{avg2}) to allow for nanoampere-level bias current. To avoid the current draw of a summing node, the outputs of the two branches are averaged (R_{avg1} and R_{avg2}) before being filtered (C_{LPF}). C_{byp} makes the node at the gate of M_{CG} appear to be a virtual ground for the input signal.

This article has been accepted for inclusion in a future issue of this journal. Content is final as presented, with the exception of pagination.

6

IEEE JOURNAL OF SOLID-STATE CIRCUITS

Fig. 9. Schematic of ripple-canceling ED. Resistors (white rectangles) implemented with PMOS pseudoresistors.
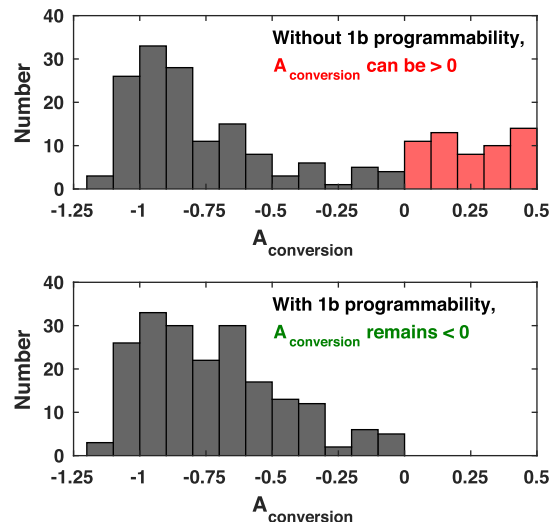

Fig. 10. Simulated ED results show robustness of the sign of the conversion gain over global process variation (200 pt. Monte Carlo). Tighter control over its magnitude can be achieved by making all ED elements programmable.

To understand second-order effects in the ripple-cancelling ED, we derive the conversion gain of the topology. Starting with the expression for the drain current of a MOSFET in subthreshold and ignoring the body effect [22]

$$I_{D,\text{subth}} \approx I_S e^{\frac{\frac{1}{n}(V_G - V_{th}) - V_S}{V_T}} \left(1 - e^{-\frac{V_{DS}}{V_T}}\right)(1 + \lambda V_{DS}) \quad (3)$$

one can average the drain current over one cycle of the input signal and subtract from that the drain current at zero input $(I_{D,q})$ to find the additional dc current due to the conversion gain of the device. Following this procedure for both the CS and CG topologies and keeping results to second order in V_{in}/V_T, we find that

$$I_{D,CS,\text{conv}} \approx \frac{1}{4}\left(\frac{V_{\text{in}}}{nV_T}\right)^2 I_{D,q} \quad (4)$$

and

$$I_{D,CG,\text{conv}} \approx \frac{1}{4}\left(\frac{V_{\text{in}}}{V_T}\right)^2 \left[1 + \frac{2}{ng_m r_o}\right.$$
$$\left. - \frac{1}{e^{V_{DS,q}/V_T} - 1}\left(3 + \frac{2}{ng_m r_o}\right)\right] I_{D,q}. \quad (5)$$

The CG expression lends a few important insights. For $V_{DS,q}/V_T \gg 1$ and $ng_m r_o \gg 1$, the term in brackets is approximately unity and the conversion gain of the CG stage becomes approximately n^2 times that of the CS stage. However, for low enough $V_{DS,q}/V_T$, the term in brackets can actually become negative. Therefore, it is imperative that M_{CG} be kept in saturation to avoid potentially reducing the conversion gain or flipping its sign (which would result in incorrect comparator decisions).

Our use of PMOS pseudoresistors makes it possible in some extreme process corners for V_{DS} of M_{CG} to fall low enough under nominal biasing conditions that the conversion gain of the CG stage does indeed flip in sign. For this proof of concept chip, we avoid this possibility by making the drain resistance of M_{CG} 1-bit controllable, just to make sure that it remains in saturation and that the conversion gain does not change sign; in production, all pseudoresistors could be replaced by banks of pseudoresistors to constrain the magnitude, not just the sign, of the conversion gain of this stage across process,

as demonstrated in [5]. This 1b configurability keeps the performance of the ED to within a reasonable range, as shown in Fig. 10. The final simulated conversion gain of the ED is provided in the Appendix. Simulations predict that in the TT corner, the sign of the ED conversion gain remains negative for V_{DD} from 0.3 to 0.8 V and for temperature from 0 °C to 70 °C.

The reference ladder to which the ED output voltage is compared also uses PMOS pseudoresistors. Its output is 9b-selectable to allow for one-time offset calibration that ensures sensitive operation despite variability of the output dc level of the ED with process. The programmability of the ladder can be used to margin for predicted voltage and temperature fluctuations by choosing a setting that backs off on sensitivity.

B. Digitization and Back End

Variation of the quiescent output dc level of the ED due to PVT concerns requires a comparator that can accept a wide range of input common-mode levels. In addition, for low power consumption, we want to operate with a low supply voltage across the entire chip. Therefore, we choose to use a double-tail latch-type comparator, a topology that can work with low voltage headroom due to the splitting of its two stages but can nevertheless accept a wide input common-mode range [23]. Schematic diagrams of the comparator and associated pulse generation logic are shown in Fig. 11, while the comparator timing diagram is shown in Fig. 12.

Because of the very low sampling frequency (around 1 kbit/s), the comparator is designed to minimize noise, offset, and energy consumption at the expense of delay. We first derive an upper limit on the input-referred noise and offset based on the desired sensitivity of the WuRx and the magnitude of other noise sources (see the Appendix). The dynamic energy consumption of this block is dependent on the total capacitance charged and discharged over the course
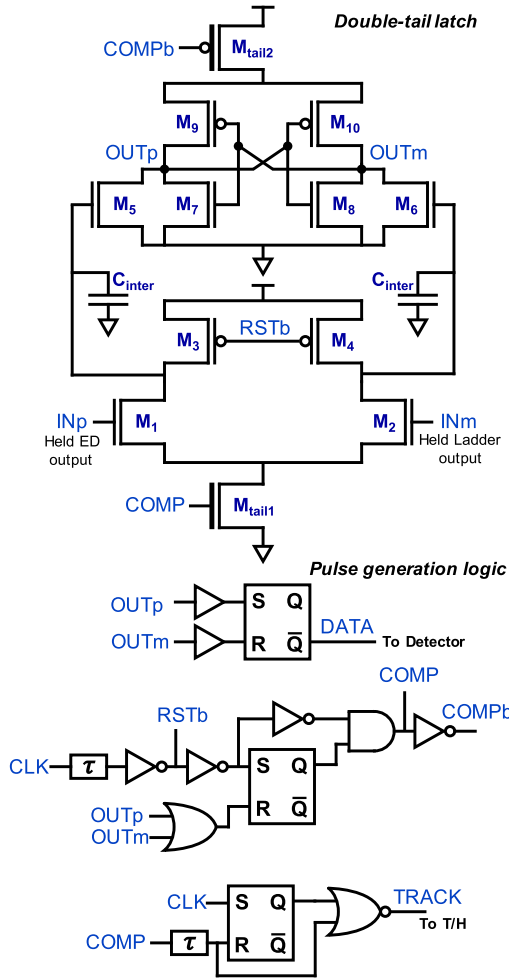
Fig. 11. Schematic of double-tail latch-type dynamic comparator and associated pulse generation logic. M_{tail1} and M_{tail2} are thick-oxide devices for leakage minimization.
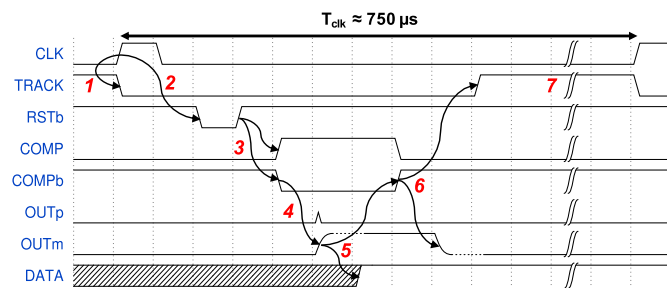

Fig. 12. Timing diagram for comparator and associated circuitry. 1—Do not track during comparison. 2—Begin by resetting comparator. 3—Once reset, begin comparison. 4—Comparator output toggles. 5—Once output toggles, end comparison; self-timing makes metastability unlikely, given large T_{clk}. 6—Comparison done, begin tracking. 7—Comparator draws only static power for majority of clock cycle.
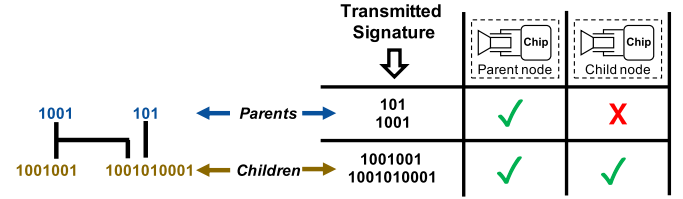

Fig. 13. Hierarchical signature detection. A parent node is awoken by both parent and child signatures; a child node is awoken by only child signatures.
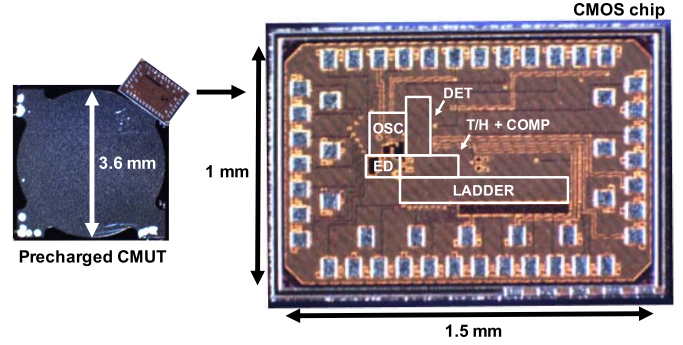

Fig. 14. Photographs of the chip die and precharged CMUT.
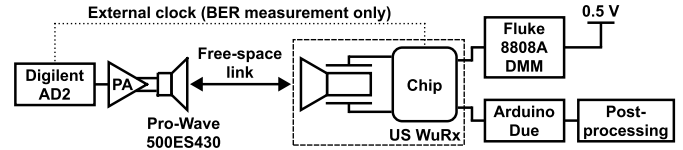

Fig. 15. Test setup; indoor measurements use a 1.4-m free-space link. The transmitter EIRP is 3.8 dBm, which corresponds to a peak generated pressure level of roughly 104.6 dB SPL, achieved 5 cm from the transmitter.
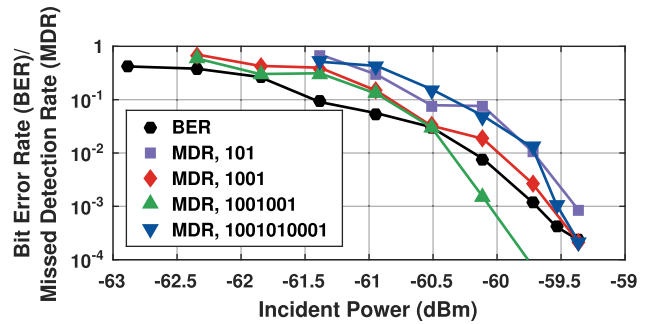

Fig. 16. Results of wireless BER and MDR measurements. The measurement floor is an error rate of 10^{-5}.

of one cycle, so we generally keep transistors small in order to minimize drawn energy, subject to meeting the noise/offset spec. We size the input pair (M_1 and M_2) so that the first stage amplifies the differential input with a gain of $\sim$10; this attenuates the noise and offset of the second stage without adding excessive noise in the first stage. For extra attenuation

of the noise and offset of the second stage, we add explicit capacitors (C_{inter}) between the stages, whose value is increased (to 75 fF) until the noise/offset spec is met. M_5–M_{10} are kept as small as possible because the delay is not a concern and because the noise and offset of this stage are considerably attenuated. Because the comparator can afford to be slow, the tail devices are also as small as possible.

The low sampling rate makes leakage a potential concern. This is combated in two ways: first, the comparator's control signals (used to start the comparison and to reset the comparator) are pulsed to keep devices off for as long as
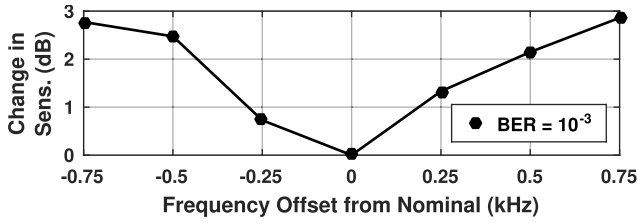
This article has been accepted for inclusion in a future issue of this journal. Content is final as presented, with the exception of pagination.

8   IEEE JOURNAL OF SOLID-STATE CIRCUITS
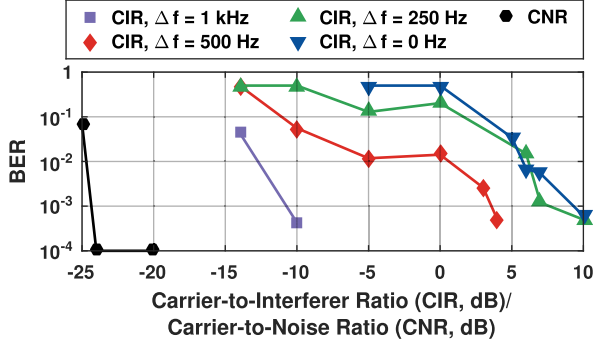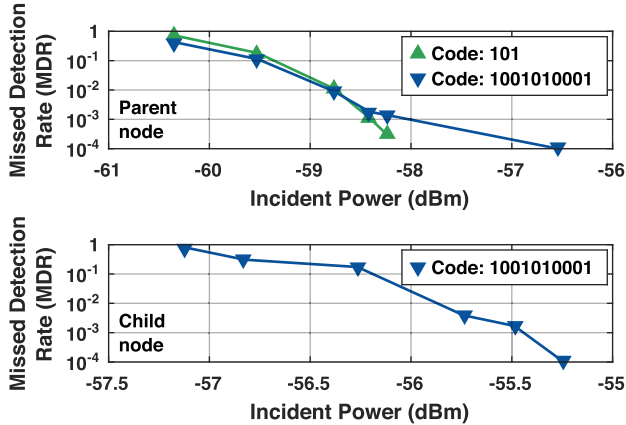

Fig. 17.   Results of wireless frequency selectivity measurements.

Fig. 18.   Results of wireless CIR and CNR measurements. CIR tests performed with a single CW interferer at a frequency Δf above the carrier. CNR tests performed with near-brickwall-filtered white noise with bandwidth 1 kHz centered at the carrier. The measurement floor is an error rate of 10^{-4}.

Fig. 19.   Results of wireless signature hierarchy measurements. For these tests, a single CMUT was shared between parent and child WuRxs to characterize hierarchical wake-up independently of CMUT/channel properties. The false alarm rate for the child node while 101 (a parent code) was being transmitted was <0.01 /s. The measurement floor is an error rate of 10^{-4}.

possible; second, the comparator's tail devices are thick-oxide FETs with extremely low leakage. The comparator is self-timed in the sense that its control signals are generated by its own output with the help of auxiliary pulse-generation logic; the comparator is almost guaranteed to decide within one clock period because of the very low sampling rate, making the probability of metastability basically zero. Simulations of the fully designed comparator predict a power consumption of 0.725 nW, an input-referred noise (rms) of 0.218 mV, and an input-referred offset (rms) of 3.7 mV.

The output of the comparator is fed into a digital signature detector implemented with a shift register. To avoid the area and power penalty of a crystal oscillator, we use a 7b-trimmable on-chip relaxation oscillator to clock the detector; the accompanying increased clock uncertainty is
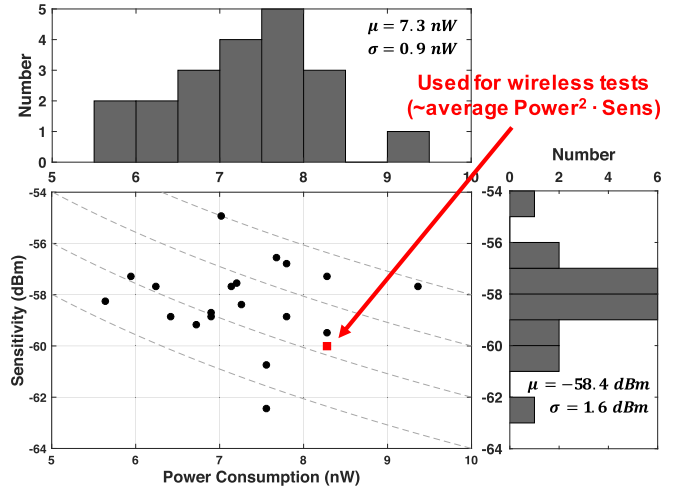
Fig. 20.   Measurements of 20 chips from the same wafer lot. These variability measurements were taken electrically (with a signal generator in place of the precharged CMUT) at 62.5 bit/s and 0.6 V. The chip used for the wireless tests whose results are shown in Figs. 16–19 was selected from this group based on its roughly average Power^2 · Sensitivity product.
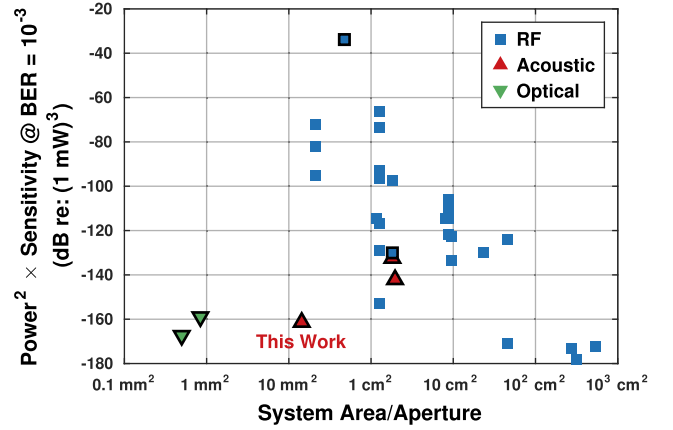
Fig. 21.   Survey of WuRxs in the literature, 2009–2018. Black outline signifies that the radiator is included in this paper and that the sum of all reported areas is, therefore, used. For all other works, a system aperture corresponding to an electrically small loop antenna of diameter $\lambda/10$ is assumed. Data available upon request.

handled by sampling the comparator output at four times the data rate and comparing every fourth output of the shift register (in parallel) with a hard-coded signature. We avoid skipping data by clocking in the opposite direction as the data flow, from the detector to the comparator and from there to the track-and-hold circuit.

The detector compares the received bits with one of four hard-coded signatures. As shown in Fig. 13, the set of signatures is designed such that the longer ("child") signatures each contain at least one of the shorter ("parent") signatures, the idea being that child nodes cannot be woken up without also waking up nearby parent nodes. This scheme provides basic hardware-level hierarchical security for very little increase in power consumption.

IV. Measurements and Benchmarking

A. Measurements

The proposed WuRx chip was fabricated in TSMC 65-nm CMOS GP technology, draws 16 nA from a 0.5 V

This article has been accepted for inclusion in a future issue of this journal. Content is final as presented, with the exception of pagination.

REKHI AND ARBABIAN: ULTRASONIC WAKE-UP WITH PRECHARGED TRANSDUCERS

9

TABLE I
COMPARISON OF THE PROPOSED WuRx WITH SELECTED PRIOR WORK

	Yadav JSSC '13	Salazar ISSCC '15	Roberts ISSCC '16	Fuketa TCAS-II '17	Jiang ISSCC '17	Sadagopan RFIC '17	Moody ISSCC '18	Abdelhamid CICC '18	This Work
Technology	65 nm	65 nm	65 nm	250 nm	180 nm	65 nm	130 nm	65 nm	**65 nm**
Wake-Up Medium	Acoustic	RF	RF	Acoustic	RF	RF	RF	RF	**Acoustic**
Carrier Frequency	40.6 kHz	2.4 GHz	2.4 GHz	41 kHz	113.5 MHz	2.4 GHz	151.8 MHz	2.4 GHz	**~57 kHz**
Data Rate	250 bit/s	10 kbit/s	~8.2 kbit/s	250 bit/s	300 bit/s	2.5 kbit/s	200 bit/s	83 kbit/s	**336 bit/s**
Power	4.4 µW	99 µW	236 nW	1 µW	4.5 nW	365 nW	7.4 nW	240 nW	**8 nW**
Sensitivity[a]	−85 dBm	−97 dBm	−56.5 dBm[b]	−82.1 dBm[c]	−65 dBm	−61.5 dBm	−76 dBm	−80 dBm	**−59.7 dBm**
Die Active Area[d]	1.24 mm^2	0.06 mm^2	2.25 mm^2	0.0064 mm^2	6 mm^2	1.1 mm^2	1.95 mm^2	0.48 mm^2	**1.5 mm^2**
System Area/Aperture[e]	178 mm^2 [f]	123 mm^2	123 mm^2	201 mm^2 [f]	54 900 mm^2	187.5 mm^2	30 700 mm^2	123 mm^2	**14.5 mm^2**
Wireless Test?	Yes	Not shown	Yes	Yes	Not shown	Yes	No	No	**Yes**
Interference Test?	Yes[g]	Yes	Not shown	No	No	Yes	Yes	No	**Yes**
Multiple Chips Measured?	Not shown	Not shown	Not shown	Not shown	Not shown	Not shown	Not shown	Not shown	**Yes: 2 (wireless) 20 (electrical)**

[a] BER = 10^{-3} [b] With coding.   [c] Estimated.   [d] If active area not reported, entire die area used.   [e] Either the sum of all reported areas (if antenna included) or $\pi(\lambda/20)^2$ (if antenna not included).   [f] Includes transducer area.   [g] Limited to interference present in ambient environment.

supply, and measures 1 mm × 1.5 mm. Both chip die and precharged CMUT are shown in Fig. 14. Because the performance of our WuRx is tightly tied to our use of ultrasound as the carrier of the wake-up signal, we perform full wireless characterization to show that the transducer and channel properties are amenable to proper wake-up operation. This includes BER measurements, missed detection rate (MDR) tests, and interference measurements (both filtered broadband noise and single-tone interferers). We also characterize multiple chips from the same wafer lot to demonstrate the robustness of our design to process variation.

Fig. 15 shows the wireless test setup; the transmitter consists of a broadband air-coupled ultrasonic transducer driven by a custom board-level power amplifier (PA). For each test, incident pressure was determined by combining the measured CMUT voltage with sensitivity data previously collected using a calibrated microphone (G.R.A.S. 40DP); incident power was then calculated by combining pressure with CMUT area. As shown in Fig. 16, synchronized BER tests establish operation at nominal sensitivity, while unsynchronized MDR tests show sensitivity within ±0.5 dB of BER results, indicating that 4× oversampling effectively mitigates detection errors due to timing uncertainty. The nominal sensitivity of −59.7 dBm corresponds to an acoustic pressure level of 80 dB SPL. Bandwidth, carrier-to-interferer ratio (CIR), and carrier-to-noise ratio (CNR) measurements, shown in Figs. 17 and 18, indicate robustness of the ultrasonic WuRx to close continuous wave (CW) interferers and narrowband noise; slight increases in BER over a short CIR range for some values of Δf likely stem from the probabilistic nature of BER measurement at the chosen data sequence length. Fig. 19 shows the results of wireless signature hierarchy measurements, confirming proper operation. Long-range (3.3 m) tests with a peak generated acoustic pressure of 112 dB SPL show wireless functionality in an outdoor setting with ambient noise and a strong 25-kHz interferer [9]. Increasing transmitter power or aperture (within regulatory constraints, as mentioned in Section II) would enable higher range.

In Fig. 20, we show sensitivity and power consumption measurements of 20 different chips from the same wafer lot. These results suggest that circuit-level sources of mismatch (including the ED variability discussed earlier) result in an acceptable chip-level performance spread. Out of these 20 chips, a chip with roughly average Power^2 · Sensitivity product was used to take the wireless measurements whose results are shown in Figs. 16–19.

B. Benchmarking

In a receiver whose power consumption is dominated by its gain stages, first-order considerations suggest that the receiver sensitivity should be inversely proportional to the square of the power consumption. A survey of the literature confirms this intuition, while also reflecting a steady improvement in the power–sensitivity tradeoff over time [6].

Sensitivity and area also have a direct tradeoff because of the dependence of radiation resistance upon transducer area, as shown in Section II. While our CMUT design method resulted in a constant Sensitivity · Area^n with $n > 1$, different area dependencies could potentially be obtained by following a different optimization procedure, using other kinds of acoustic transducers, or working with electromagnetic antennas. To include area in our benchmarking without making assumptions about the value of n across different works, in Fig. 21, we plot the Power^2 · Sensitivity of WuRxs against their total system area. Specific area-sensitivity relationships can be explored by superimposing trend lines on the plot, while area-agnostic comparisons, relevant where the WuRx has a small die area and uses an existing antenna in the system, can be made by ignoring the area axis. Most prior work does not include or state the area of the radiator; for those works, an electrically small loop antenna of diameter $\lambda/10$ was assumed, along with the lines of [24].

Fig. 21 shows that the proposed WuRx is the smallest among all RF/acoustic WuRxs and achieves the lowest Power^2 · Sensitivity product among RF/acoustic WuRxs

smaller than 10 cm^2. While published optical WuRxs consume less power (<1nW) and are smaller (often single chip with integrated photodiode), their need for a steered laser at long range and their sensitivity to ambient light puts them in a different use case category. Table I compares this paper with selected prior RF/acoustic systems in more detail [5], [9], [24]–[30].

V. CONCLUSION

We presented an ultrasonic WuRx that uses a precharged CMUT and a CMOS ED-first front end to achieve a sensitivity of −59.7 dBm at a power consumption of 8 nW and a total area of 14.5 mm^2. Through CMUT design optimization, we showed that the transducer can be further miniaturized without changing the operation frequency, found the degradation in sensitivity associated with doing so, and tied this degradation to the transducer impedance. We also discussed the need for and our method of ripple cancellation during envelope detection. In the Appendix, we investigate the prospects of improving sensitivity by including a simple, low-power LNA before the ED while keeping the power budget below 10 nW. We demonstrated the working operation of the proposed WuRx with wireless BER, MDR, CIR, CNR, and signature hierarchy measurements, and benchmarked our system against the literature. Our work demonstrates that using ultrasound as a carrier for wake-up enables miniaturized, long-range, low-power WuRxs that are competitive with RF-based solutions and are particularly attractive for next-generation IoT nodes.

APPENDIX
INCLUDING A NANOWATT LNA

One can conjecture that due to the relatively low carrier frequency used in this system, it may be possible to provide amplification at the carrier for very little additional current and, therefore, achieve a net improvement in the Power^2 · Sensitivity product while staying within the nanowatt power consumption regime. In this appendix, we investigate this claim to first order. Fig. 22 shows the two topologies that we compare.

The first topology, which is the one implemented in this paper, achieves an SNR of

$$\text{SNR}_1 = \frac{\frac{1}{2}v_{\text{CMUT}}^2}{\overline{v_{n,\text{CMUT,out}}^2} + \frac{1}{A_{\text{conv}}^2}\overline{v_{n,\text{at comp,out}}^2}} \tag{A.1}$$

where v_{CMUT} is the peak signal level at the output of the CMUT, $\overline{v_{n,\text{CMUT,out}}^2}$ is the output-referred total integrated CMUT noise, A_{conv} is the conversion gain of the ED, and $\overline{v_{n,\text{at comp,tot}}^2}$ is the TIN at the comparator input due to ED noise, reference ladder noise, and comparator noise and offset. Meanwhile, the second topology achieves an SNR of

$$\text{SNR}_2 = \frac{1}{2}v_{\text{CMUT}}^2 \Bigg/ \Bigg(\overline{v_{n,\text{CMUT,out}}^2} + \frac{1}{A^2}\overline{v_{n,\text{LNA,out}}^2}$$
$$+ \frac{1}{A^2 A_{\text{conv}}^2}\overline{v_{n,\text{at comp,out}}^2}\Bigg) \tag{A.2}$$
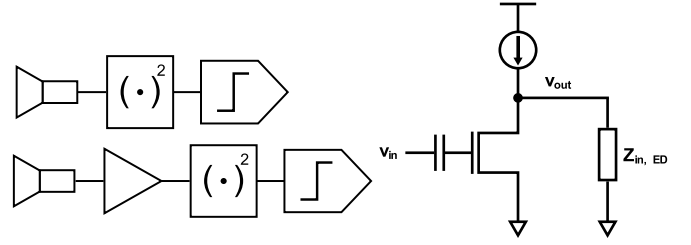

Fig. 22. The two topologies compared: without LNA (top left) and with LNA (bottom left). Schematic of the LNA used in this comparison; biasing details not shown (right).
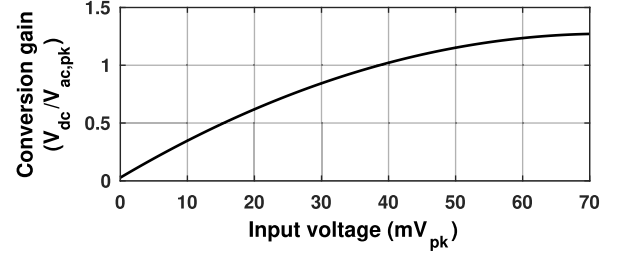

Fig. 23. Variation of ED conversion gain with input amplitude (simulated).

where $\overline{v_{n,\text{LNA,out}}^2}$ is the output-referred total integrated LNA noise and A is the gain of the LNA. To keep the scope of the comparison tractable, we compare the two topologies without redesigning the non-LNA parts of the receiver; this may leave some performance on the table but makes it possible to simply substitute values for gain and noise from the implemented WuRx for a first-order understanding of possible improvement. Based on simulations, $\overline{v_{n,\text{CMUT,out}}^2} \approx 4.7 \times 10^{-12}$ V^2, $\overline{v_{n,\text{at comp,out}}^2} \approx 1.5 \times 10^{-5}$ V^2 (dominated by comparator offset), and A_{conv} varies with ED input signal amplitude as shown in Fig. 23.

For this paper, we consider a very simple LNA: the CS maximum possible transconductance efficiency—this is enabled by the lack of need for bandwidth relative to RF-based WuRxs. Making use of the fact that $g_m/I_D = 1/(nV_T)$ in subthreshold, the low-frequency gain of this stage is

$$A = -g_m(r_o||Z_{\text{in,ED}}) = -\frac{I_D}{nV_T}(r_o||Z_{\text{in,ED}}) \tag{A.3}$$

and its output-referred current noise power spectral density is

$$\overline{i_{n,d}^2} = \left(2kTng_m + \frac{K_f}{f}\frac{g_m^2}{\text{WLC}_{\text{ox}}^2}\right)\Delta f$$
$$= \left(I_D \cdot 2q + \left(\frac{I_D}{nV_T}\right)^2\frac{K_f/f}{\text{WLC}_{\text{ox}}^2}\right)\Delta f \tag{A.4}$$

making its output-referred voltage noise power spectral density equal to

$$\overline{v_{n,d}^2} = |r_o||Z_{\text{in,ED}}|^2\left(I_D \cdot 2q + \left(\frac{I_D}{nV_T}\right)^2\frac{K_f/f}{WLC_{\text{ox}}^2}\right)\Delta f. \tag{A.5}$$

We construct the comparison by sweeping over LNA bias current. For each value of the bias current, we determine the transistor width that satisfies the chosen g_m/I_D (∼30 S/A,
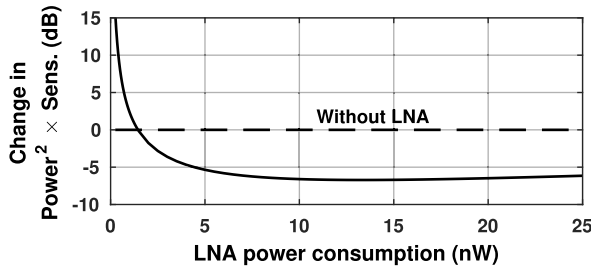
Fig. 24. Results of first-order investigation of the addition of a simple, low-power LNA to the presented ultrasonic WuRx.

the maximum in the 65-nm process used) assuming a length of 1 μm (chosen for high intrinsic gain and because not f_T-limited). With these parameters and the simulated input impedance of the ED over frequency, we calculate the LNA gain and noise (assuming a 1 h observation interval for flicker noise) and then solve for the minimum input signal power level required to achieve the SNR set by the BER specification. This SNR is derived by combining the facts that BER = $Q(v_{\text{sig,pk}}/v_{\text{noise,rms}})$ and SNR = $(1/2)v_{\text{sig,pk}}^2/v_{\text{noise,rms}}^2$ to arrive at SNR = $(1/2)[Q^{-1}(\text{BER})]^2$. The change in sensitivity (in dB) created by the introduction of the LNA is then added to the change in the square of the total WuRx power consumption (in dB) and the resultant change in the Power^2 · Sensitivity product is plotted against the LNA power consumption.

Fig. 24 shows this plot, which reveals that the introduction of a simple single-stage LNA, without modification of any other stage, can improve the Power^2 · Sensitivity product by as much as 6.7 dB if doubling or tripling the total WuRx power consumption is acceptable. However, if the power consumption is to be kept below 10 nW, then this simple scheme can only improve the product by ∼1.8 dB. These results suggest that if only a little more power is to be expended, it may pay off to first reduce the dominant SNR-limiting factor (currently the comparator offset) before including an LNA, despite the low carrier frequency used.

Acknowledgment

References

[1] D. Evans, "The Internet of Things: How the next evolution of the Internet is changing everything," Cisco, San Jose, CA, USA, Tech. Rep., Apr. 2011.

[2] P. Jonsson et al., "Ericsson mobility report June 2018," Ericsson, Stockholm, Sweden, Tech. Rep., 2018. [Online]. Available: www.ericsson.com/mobility-report

[3] C. Guo, L. C. Zhong, and J. M. Rabaey, "Low power distributed MAC for ad hoc sensor radio networks," in Proc. IEEE Global Telecommun. Conf. (GLOBECOM), San Antonio, TX, USA, Nov. 2001, pp. 2944–2948.

[4] N. Pletcher, S. Gambini, and J. Rabaey, "A 65 μW, 1.9 GHz RF to digital baseband wakeup receiver for wireless sensor nodes," in Proc. IEEE Custom Integr. Circuits Conf., San Jose, CA, USA, Sep. 2007, pp. 539–542.

[5] H. Jiang et al., "A 4.5 nW wake-up radio with −69 dBm sensitivity," in IEEE ISSCC Dig. Tech. Papers, San Francisco, CA, USA, Feb. 2017, pp. 416–417.

[6] D. D. Wentzloff, Low Power Radio Survey. [Online]. Available: www.eecs.umich.edu/wics/low_power_radio_survey.html

[7] J. Charthad, N. Dolatsha, A. Rekhi, and A. Arbabian, "System-level analysis of far-field radio frequency power delivery for mm-sized sensor nodes," IEEE Trans. Circuits Syst. I, Reg. Papers, vol. 63, no. 2, pp. 300–311, Feb. 2016.

[8] M. Tabesh, N. Dolatsha, A. Arbabian, and A. M. Niknejad, "A power-harvesting pad-less millimeter-sized radio," IEEE J. Solid-State Circuits, vol. 50, no. 4, pp. 962–977, Apr. 2015.

[9] A. S. Rekhi and A. Arbabian, "A 14.5 mm^2 8 nW −59.7 dBm-sensitivity ultrasonic wake-up receiver for power-, area-, and interference-constrained applications," in IEEE ISSCC Dig. Tech. Papers, vol. 61, 2018, pp. 454–456.

[10] A. S. Rekhi, B. T. Khuri-Yakub, and A. Arbabian, "Wireless power transfer to millimeter-sized nodes using airborne ultrasound," IEEE Trans. Ultrason., Ferroelectr., Freq. Control, vol. 64, no. 1, pp. 1526–1541, Oct. 2017.

[11] H. Köymen et al., "An improved lumped element nonlinear circuit model for a circular CMUT cell," IEEE Trans. Ultrason., Ferroelectr., Freq. Control, vol. 59, no. 8, pp. 1791–1799, Aug. 2012.

[12] I. Ladabaum, X. Jin, H. T. Soh, A. Atalar, and B. T. Khuri-Yakub, "Surface micromachined capacitive ultrasonic transducers," IEEE Trans. Ultrason., Ferroelect., Freq. Control, vol. 45, no. 3, pp. 678–690, May 1998.

[13] M.-C. Ho, M. Kupnik, K. K. Park, and B. T. Khuri-Yakub, "Long-term measurement results of pre-charged CMUTs with zero external bias operation," in Proc. IEEE Int. Ultrason. Symp., Dresden, Germany, Oct. 2012, pp. 89–92.

[14] H. Köymen, A. Atalar, S. Güler, I. Köymen, A. S. Tasdelen, and A. Ünlügedik, "Unbiased charged circular CMUT microphone: Lumped-element modeling and performance," IEEE Trans. Ultrason., Ferroelectr., Freq. Control, vol. 65, no. 1, pp. 60–71, Jan. 2018.

[15] C. R. Chappidi and K. Sengupta, "Globally optimal matching networks with lossy passives and efficiency bounds," IEEE Trans. Circuits Syst. I, Reg. Papers, vol. 65, no. 1, pp. 257–269, Jan. 2018.

[16] T. C. Chang, M. J. Weber, M. L. Wang, J. Charthad, B. T. Khuri-Yakub, and A. Arbabian, "Design of tunable ultrasonic receivers for efficient powering of implantable medical devices with reconfigurable power loads," IEEE Trans. Ultrason., Ferroelect., Freq. Control, vol. 63, no. 10, pp. 1554–1562, Oct. 2016.

[17] A. Nikoozadeh, "Intracardiac ultrasound imaging using capacitive micromachined ultrasonic transducer (CMUT) Arrays," Dept. Elect. Eng., Ph.D. dissertation, Stanford Univ., Stanford, CA, USA, 2010.

[18] K. K. Park, H. J. Lee, P. Crisman, M. Kupnik, O. Oralkan, and B. T. Khuri-Yakub, "Optimum design of circular CMUT membranes for high quality factor in air," in Proc. IEEE Ultrason. Symp., Beijing, China, Nov. 2008, pp. 504–507.

[19] C. A. Balanis, Antenna Theory: Analysis and Design, 3rd ed. Hoboken, NJ, USA: Wiley, 2005.

[20] R. Kubo, "The fluctuation-dissipation theorem," Reports Progr. Phys., vol. 29, no. 1, pp. 255–284, 1966.

[21] K.-W. Cheng and S.-E. Chen, "An ultralow-power wake-up receiver based on direct active RF detection," IEEE Trans. Circuits Syst. I, Reg. Papers, vol. 64, no. 7, pp. 1661–1672, Jul. 2017.

[22] B. Degnan. Wikipedia-Fails-Subvt. [Online]. Available: https://sites.google.com/site/degnan68k/semiconductors/wikipedia-fails-subvt

[23] D. Schinkel, E. Mensink, E. Klumperink, E. van Tuijl, and B. Nauta, "A double-tail latch-type voltage sense amplifier with 18ps setup+hold time," in IEEE ISSCC Dig. Tech. Papers, San Francisco, CA, USA, Feb. 2007, pp. 314–315.

[24] K. R. Sadagopan, J. Kang, S. Jain, Y. Ramadass, and A. Natarajan, "A 365 nW -61.5 dBm sensitivity, 1.875 cm^2 2.4 GHz wake-up receiver with rectifier-antenna co-design for passive gain," in Proc. IEEE Radio Freq. Integr. Circuits Symp. (RFIC), Honolulu, HI, USA, Jun. 2017, pp. 180–183.

[25] K. Yadav, I. Kymissis, and P. R. Kinget, "A 4.4-μW wake-up receiver using ultrasound data," IEEE J. Solid-State Circuits, vol. 48, no. 3, pp. 649–660, Mar. 2013.

[26] C. Salazar, A. Kaiser, A. Cathelin, and J. Rabaey, "A −97 dBm-sensitivity interferer-resilient 2.4 GHz wake-up receiver using dual-IF multi-N-path architecture in 65 nm CMOS," in IEEE ISSCC Dig. Tech. Papers, San Francisco, CA, USA, vol. 58, Feb. 2015, pp. 242–243.

[27] N. E. Roberts et al., "A 236 nW -56.5 dBm-sensitivity bluetooth low-energy wakeup receiver with energy harvesting in 65 nm CMOS," in IEEE ISSCC Dig. Tech. Papers, San Francisco, CA, USA, vol. 59, Jan./Feb. 2016, pp. 450–451.

[28] H. Fuketa, S. O'uchi, and T. Matsukawa, "A 0.3-V 1-μW super-regenerative ultrasound wake-up receiver with power scalability," *IEEE Trans. Circuits Syst., II, Exp. Briefs*, vol. 64, no. 9, pp. 1027–1031, Sep. 2017.

[29] J. Moody *et al.*, "A −76 dBm 7.4 nW wakeup radio with automatic offset compensation," *IEEE ISSCC Dig. Tech. Papers*, vol. 61, pp. 452–454, 2018.

[30] M. R. Abdelhamid, A. Paidimarri, and A. P. Chandrakasan, "A −80 dBm BLE-compliant, FSK wake-up receiver with system and within-bit dutycycling for scalable power and latency," in *Proc. IEEE Custom Integr. Circuits Conf. (CICC)*, Apr. 2018, pp. 1–4.

Angad S. Rekhi (S'13) received the B.S. degree in electrical engineering from Caltech, Pasadena, CA, USA, in 2014, and the M.S. degree in electrical engineering from Stanford University, Stanford, CA, USA, in 2016, where he is currently pursuing the Ph.D. degree in electrical engineering, under the supervision of Prof. A. Arbabian. His Ph.D. thesis is on ultrasound-assisted wireless connectivity for next-generation IoT devices.

From 2012 to 2014, he worked with Prof. A. Hajimiri at Caltech, where he designed and tested integrated electronic-photonic systems. In 2018, he was with the Circuits Research Group, NVIDIA Research, Santa Clara, CA, USA, where he designed analog/mixed-signal hardware for machine learning. In addition to his thesis work, his work at Stanford University has included the investigation of a novel form of neurostimulation.

Mr. Rekhi was a recipient of the NSF GRFP in 2014, the NDSEG Fellowship in 2016, the ADI Outstanding Student Designer Award in 2014 and 2018, and the IEEE SSCS Predoctoral Achievement Award in 2019.

Amin Arbabian (S'06–M'12–SM'17) received the Ph.D. degree in electrical engineering and computer science from the University of California at Berkeley, Berkeley, CA, USA, in 2011.

From 2007 to 2008, he was a part of the Initial Engineering Team, Tagarray, Inc., Palo Alto, CA, USA. In 2010, he joined the Qualcomm's Corporate Research and Development Division, San Diego, CA, USA, where he designed circuits for next-generation ultralow power wireless transceivers. In 2012, he joined Stanford University, Stanford, CA, USA, as an Assistant Professor of electrical engineering. His current research interests include mm-wave and high-frequency circuits and systems, imaging technologies, Internet of Everything devices including wireless power delivery techniques, and medical implants.

Dr. Arbabian was a recipient or co-recipient of the 2016 Stanford University Tau Beta Pi Award for Excellence in Undergraduate Teaching, the 2015 NSF CAREER Award, the 2014 DARPA Young Faculty Award including the Director's Fellowship in 2016, the 2013 Hellman Faculty Scholarship, the 2010–2011, 2014–2015, and 2016–2017 Qualcomm Innovation Fellowships, and best paper awards at the 2017 IEEE Biomedical Circuits and Systems Conference, the 2016 IEEE Conference on Biomedical Wireless Technologies, Networks, and Sensing Systems, the 2014 IEEE VLSI Circuits Symposium, the 2013 IEEE International Conference on Ultra-Wideband, the 2010 IEEE Jack Kilby Award for Outstanding Student Paper at the International Solid-State Circuits Conference, and two-time second place best student paper awards at 2008 and 2011 RFIC Symposiums. He currently serves on the steering committee for RFIC Symposium, the technical program committees of RFIC Symposium, ESSCIRC, CICC, and VLSI Circuits Symposium, and as an Associate Editor for IEEE SOLID-STATE CIRCUITS LETTERS and the *IEEE Journal of Electromagnetics, RF and Microwaves in Medicine and Biology*.